

Resonance, Velocity, Dispersion, and Attenuation of Ultrasound-Induced Shear Wave Propagation in Blood Clot In Vitro Models

Guillaume Bosio, BSc, François Destrempes, PhD, Ladan Yazdani, PhD, Marie-Hélène Roy Cardinal, PhD, Guy Cloutier, BEng, PhD 

Received May 23, 2023, from the Institute of Biomedical Engineering, University of Montreal, Montreal, Quebec, Canada (G.B., L.Y., G.C.); Laboratory of Biorheology and Medical Ultrasonics, University of Montreal Hospital Research Center (CRCHUM), Montreal, Quebec, Canada (G.B., F.D., L.Y., M.-H.R.C., G.C.); and Department of Radiology, Radio-Oncology and Nuclear Medicine, University of Montreal, Montreal, Quebec, Canada (G.C.). Manuscript accepted for publication November 25, 2023.

Authors recognize the guidance provided by Dr Manish Bhatt at the beginning of the project. This study was financed by the Natural Sciences and Engineering Research Council of Canada (#2022-03729). All authors of this article have reported no disclosures.

The authors declare no potential conflict of interest.

Address correspondence to Guy Cloutier, Centre de Recherche du Centre Hospitalier de l'Université de Montréal, Tour Viger (local R11-464), 900 rue Saint-Denis, Montréal, QC H2X 0A9, Canada.

E-mail: guy.cloutier@umontreal.ca

Abbreviations

ρ , tissue density; 2P-FS, two-points frequencyshift; AMUSE, attenuation measuring ultrasound shear wave elastography; ANOVA, analysis of variance; A-RANSAC, adaptive random sample consensus; ARFI, acoustic radiation force impulse; ARFIRE, acoustic radiation force induced resonance elastography; c_s , shear wave velocity; CV, coefficient of variation; d , average distance between pairs of frequency resonant peaks; E , Young modulus; f_1 , frequency of the main resonant peak; FS, frequency shift; LMM, linear mixed effect model; np , number of peaks; R^2 , coefficient of determination; RF, radio frequency; R-FS, revisited frequency shift; ROI, region-of-interest; SW, shear wave; SWIRE, shear wave induced resonance elastography; TE, transient elastography; w_1 , width at half maximum of the main resonant peak; $w_{1/2}$, half-width of the spectral peak

doi:10.1002/jum.16387

This is an open access article under the terms of the [Creative Commons Attribution](https://creativecommons.org/licenses/by/4.0/) License, which permits use, distribution and reproduction in any medium, provided the original work is properly cited.

Objective—Improve the characterization of mechanical properties of blood clots. Parameters derived from shear wave (SW) velocity and SW amplitude spectra were determined for gel phantoms and in vitro blood clots.

Methods—Homogeneous phantoms and phantoms with gel or blood clot inclusions of different diameters and mechanical properties were analyzed. SW amplitude spectra were used to observe resonant peaks. Parameters derived from those resonant peaks were related to mimicked blood clot properties. Three regions of interest were tested to analyze where resonances occurred the most. For blood experiments, 20 samples from different pigs were analyzed over time during a 110-minute coagulation period using the Young modulus, SW frequency dispersion, and SW attenuation.

Results—The mechanical resonance was manifested by an increase in the number of SW spectral peaks as the inclusion diameter was reduced ($P < .001$). In blood clot inclusions, the Young modulus increased over time during coagulation ($P < .001$). Descriptive spectral parameters (frequency peak, bandwidth, and distance between resonant peaks) were linearly correlated with clot elasticity values ($P < .001$) with $R^2 = .77$ for the frequency peak, .60 for the bandwidth, and .48 for the distance between peaks. The SW dispersion and SW attenuation reflecting the viscous behavior of blood clots decreased over time ($P < .001$), mainly in the early stage of coagulation (first minutes).

Conclusion—The confined soft inclusion configuration favored SW mechanical resonances potentially challenging the computation of spectral-based parameters, such as the SW attenuation. The impact of resonances can be reduced by properly selecting the region of interest for data analysis.

Key Words—blood clot; shear wave attenuation; shear wave dispersion; shear wave elastography; shear wave speed; spectral resonance; ultrasound

Ultrasound elastography is used to estimate the stiffness of biological tissues. Several methods have been developed such as strain elastography,^{1–8} dynamic elastography,^{6–13} or resonance elastography in the context of soft inclusions surrounded by stiffer tissues.^{14–16} Strain elastography uses the deformation subjected to the probe's pressure exerted by a clinician to find differences in stiffness. Other strain imaging methods use the natural pulsation of organs induced by the cardiac pulse pressure.^{17–21} Dynamic methods mainly consider purely elastic solids using the

relationship $E = 3\rho c_s^2$, where E is the Young modulus, ρ the tissue density, and c_s the shear wave (SW) velocity. Among dynamic methods are transient elastography (TE),^{22,23} SW elastography,^{24–26} and acoustic radiation force impulse (ARFI) elastography,^{27,28} which display the velocity (m/s) or Young modulus (kPa) (see Refs. 6–8, 13, 29 for more details on methods).

With dynamic methods, a displacement map is calculated, and time-of-flight algorithms are used to compute the SW group velocity in the case of elastic methods, and the phase velocity in the case of viscoelastic measurements. These methods are mainly designed for measurements on large homogeneous organs such as the liver, in which wave reflections and resonance phenomena are not expected. These methods usually use directional filtering to alleviate the impact of SW reflections.^{30,31} The SW-induced resonance elastography (SWIRE) method uses the resonance of cylindrical inclusions to calculate their elasticity or viscoelasticity.^{14,15} SWIRE requires an external vibrator that excites the material at many frequencies to find resonance peaks and estimates the elasticity at these frequencies (by solving an inverse problem) and/or the viscosity (with a rheological model). Acoustic radiation force-induced resonance elastography (ARFIRE) uses the same principle as SWIRE but with a SW generated by an ultrasonic push.¹⁶ The frequency and bandwidth of the first resonant peak in the amplitude spectrum are used to compute viscoelastic parameters.

Other dynamic methods considering viscoelastic solids are based on the SW frequency dispersion, rheological modeling of the SW velocity, SW attenuation, and determination of the complex shear modulus.^{25,32–39} Most studies have focused on the dispersion and attenuation of SWs as additional parameters to complement the SW speed or Young modulus to characterize biological tissues.^{35,38–44} The dispersion is the variation of the SW speed with frequency. The SW attenuation is an inherent property of tissues related to the damping of SWs in viscoelastic solids. Recent developments on SW attenuation are based on the attenuation measuring ultrasound SW elastography (AMUSE) method,³⁵ the frequency shift (FS) method,³⁹ and its derivatives: the two-point frequency shift (2P-FS)³⁶ and the revisited frequency shift (R-FS)³³ methods. The advantage of FS-based

methods is to provide a SW attenuation map reflecting tissue viscosity. However, these methods can be sensitive to noise, and for cylindrical geometries embedding a soft inclusion, spectral resonances may further induce variability.

One of the resonance characteristics is the presence of several peaks in the amplitude spectrum (of the SW displacement over frequency).¹⁴ In homogeneous tissues, only one peak is expected.³⁹ Clots within blood vessels have a geometry and a viscoelasticity contrast favoring the presence of SW resonances. Studies on the viscoelasticity of clots have shown that as clots form and age, their Young modulus increase.^{9,45,46} Age from diagnosis is the main criterion for classifying between acute, subacute, as well as chronic thrombi.^{47,48} The treatment applied to the patient depends on this classification.^{47,48} The age of the clot is calculated according to the onset of symptoms experienced by the patient, and may therefore be subject to error. Characterizing thrombi by their age, linked to the Young modulus, SW dispersion or SW attenuation could help classify them and hence improve their management. The elasticity increase has also been linked with thrombus resistance to lysis.⁴⁹ Other teams have focused on the impact of treatments on mechanical properties, however, results on Young modulus alone have not reached a consensus.^{50,51} In their work using ARFIRE, Bhatt et al¹⁶ showed with simulated data that the first resonance peak increases in frequency as the elasticity of the inclusion is raised.

This study aimed to investigate experimentally resonance phenomena in cylindrical soft inclusions to better understand the link with inclusion's properties, as well as to evaluate the impact of resonances on the calculation of the SW dispersion and SW attenuation. Dispersion had briefly been reported in blood clots showing potential to differentiate clots of different hematocrit.^{52,53} To our knowledge, the SW attenuation has not been reported yet in blood clots. We hypothesize that resonances are caused by the reflection and reverberation of SWs at the interface between two media. We also hypothesize that they do not have time to occur when measurements are centered in the inclusion and close to the induced radiation pressure pushes. This latter hypothesis was tested by selecting several regions of interest (ROI) within phantom inclusions. The addition of SW dispersion and SW attenuation could improve the

characterization of the age of blood clots, which is currently limited clinically to the onset of symptoms and to research on the Young modulus. The spectral resonance phenomenon and how to minimize it have been addressed for the first time in this study.

Methods

Experiments were conducted on three types of phantoms: homogeneous gel phantoms without any inclusion, gel phantoms with a gel inclusion, and gel phantoms with a blood clot inclusion. Gel inclusions of different diameters were investigated.

Gel Phantom Preparation

The phantoms were made following the recipe of Bhatt et al.¹⁶ The surrounding phantom was designed to be stiffer than the blood clot or gel inclusion. It was made of 4% gelatin powder (product number G-1890, Sigma Chemical, Saint-Louis, MO), 1.5% agar (product number A-9799, Sigma Chemical), and 0.9% salt. The salt was used to avoid hypotonicity and cell swelling at phantom-blood interfaces. A softer homogeneous phantom and softer phantom inclusions were made by lowering the gelatin powder proportion to 2%. The purpose of soft inclusions was to approach mechanical properties of blood clots. Different gel inclusion diameters were studied to mimic deep vein thrombosis conditions.

Blood Clot Preparation

Porcine blood was collected at the animal facility of the University of Montreal Hospital Research Center (Montréal, QC, Canada) and anticoagulated with a sodium citrated solution at a mass ratio of 1/9. Pigs were brought in as part of an experimental protocol,⁵⁴ and only a small quantity of blood (10 mL) was collected before any drugs were given to the animal. The pigs all came from the same farm and are Yorkshire/Landrace hybrids. The hematocrit was set to 40%, and recalcification was obtained by adding CaCl_2 to a concentration of 16.1 mM ⁴⁹ to allow blood to coagulate while pouring it into the phantom inclusion. Acquisitions were performed during clotting and hardening over a 110-minute period. Clots were prepared from collected blood of 20 different pigs.

Experimental Setup

The liquid phantom was poured into a 1 L^2 container. A cylinder of 12 mm was dipped into the liquid phantom and was removed after gelation to define the geometry of the inclusion. The blood or inclusion gel was then poured into the cavity created by the cylinder. An additional soft homogeneous phantom was also prepared. Ultrasound SW-induced elastography measurements were made with a Verasonics system (Verasonics V1, Verasonics Inc., Redmond, WA) using a linear array probe (ATL L7-4, Philips, Bothell, WA), as seen in Figure 1. The position of the probe relative to the clot was adjusted to obtain the maximum clot diameter on B-mode imaging. For gel phantom experiments, additional inclusion diameters were considered (6 and 18 mm). Inclusions were located at depths of 20–40 mm on the x -axis (Figure 1), which corresponds to typical ranges of induced radiation pressure pushes in SW elastography.^{55,56} For averaging purposes, four acquisitions were performed on the homogeneous phantom and phantoms with inclusions. In the case of blood clot inclusions, acquisitions were obtained every 4 minutes during 110 minutes. The central frequency of the probe was 5 MHz, the maximum depth (here x because the probe was on the side) of the image was 51 mm, and the width (here z) was 35.6 mm. Each push duration lasted 115 μs and adjacent pushes were separated by 3 mm in the depth direction. Pushes were focused using 64 probe elements centered on the 32nd element. The depth location of pushes (total of 3 pushes) covered a range of 20–35 mm, with f -numbers varying from 1.1 to 1.9.

Data Acquisition and Post-Processing

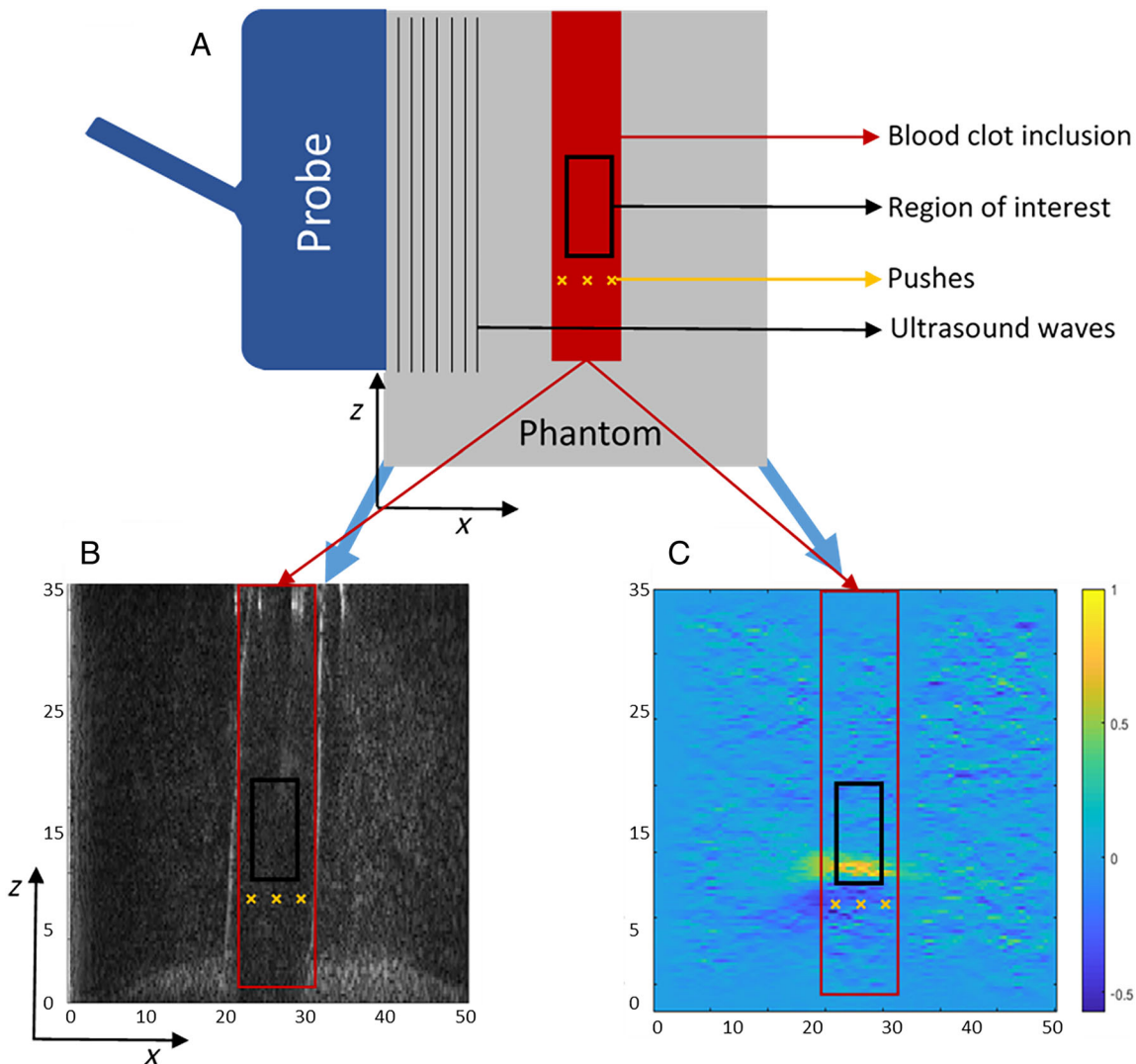
Ultrasound radio frequency (RF) signals were acquired during SW propagation. Each set of acquisitions consisted of 10 consecutive sequences at the three push locations each followed by ultrafast tracking over 100 images (at 4000 images per second). RF migrated signals⁵⁷ were converted to B-mode images for display purposes. Time-varying SW velocity maps were obtained for each sequence using the two-dimensional autocorrelation approach,⁵⁸ and averaged over the 10 acquisitions. Three ROIs were positioned manually for each clot or gel inclusion based on one B-mode image and the display of the average SW velocity map. The ROI #1 was positioned within the

inclusion, had a 5-mm width (150 pixels) in the x -direction (push line axis), and a 10-mm (40 pixels) height in the z -direction (SW propagation direction). ROI #2 had the same width as ROI #1, and half of its height in the z -direction. ROI #3 was reduced in width by 1.7 mm (50 pixels) in the x -direction, and had the same height as ROI #2 in the z -direction.

For computation of the Young modulus, the SW group velocity within a given ROI was averaged along the x -axis, as in Ref. 59. A single value was then calculated

using a time-of-flight method, after applying a directional spatial filter in the SW propagation direction.³⁰ Examples of space–time maps of the displacement are plotted in Figure 2 for the different conditions. Likewise, the phase velocity was evaluated as a function of frequency to assess viscoelastic dispersion.⁵⁹ In this case, a low-pass filter (500 Hz) was used to remove undesired noises at high frequencies. A pictorial description of the SW dispersion calculation based on the work of Deffieux et al⁵⁹ is presented in Figure 3, A and B. Measurements were done by

Figure 1. **A**, Experimental setup corresponding to a gel phantom with a blood clot inclusion, **B**, a reconstructed B-mode image with the region-of-interest (ROI in black), and **C**, a velocity map at $t = 4$ ms after the radiation pressure push, the color bar corresponds to the normalized displacement speed. Axes are in mm, x is the push line direction, and z the shear wave propagation direction.



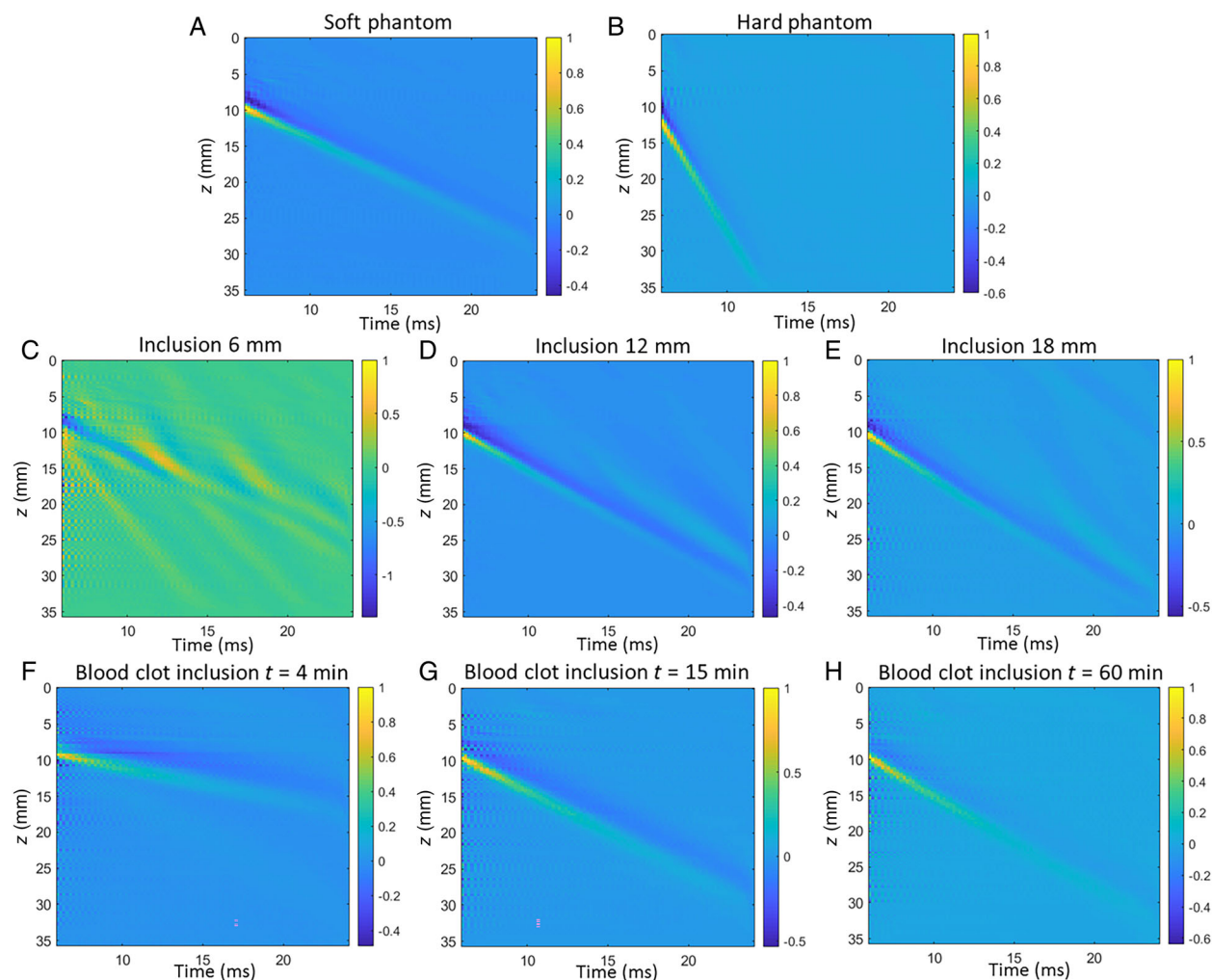
considering 9 lateral pixels corresponding to a distance of 2.25 mm. The frequency range for computing SW dispersion was selected between 50 and 500 Hz.^{32,41} The dispersion was assessed as the slope of the phase velocity along selected frequencies.

SW attenuation maps related to tissue viscosity were computed with the R-FS method.³³ With this method, the Fourier transform of the SW particle displacement velocity is taken at each position within the ROI, and assumes that the resulting amplitude spectrum fits a single gamma distribution. Shape and rate parameters of the gamma distribution are obtained by

a linear curve fitting (A-RANSAC method³³) over a distance of 2.25 mm. The SW attenuation then corresponds to the slope of the rate parameter of the gamma distribution along the SW propagation direction. Panels C and D of Figure 3 illustrate the computation of the SW attenuation; for more details, the reader can refer to Bernard et al³⁹ and Yazdani et al.³³ SW attenuation involved gamma fitting over frequencies below 1000 Hz (low-pass filtering at 500 Hz was nevertheless applied).

In the case of soft inclusions, as introduced earlier, SW displacement amplitude spectra may exhibit

Figure 2. A–H, Space–time images of SW displacements. Color bars represent the normalized amplitude of the displacement. Displacements have been averaged along the z direction inside the ROI. First milliseconds were removed because they correspond to frames of radiation force pushes. Only one direction of propagation can be seen because of the directional filter. Slopes of the yellow/blue “lines” are linked to the group velocity. The blood clot represented in panels F, G, and H corresponds to the pig #20.

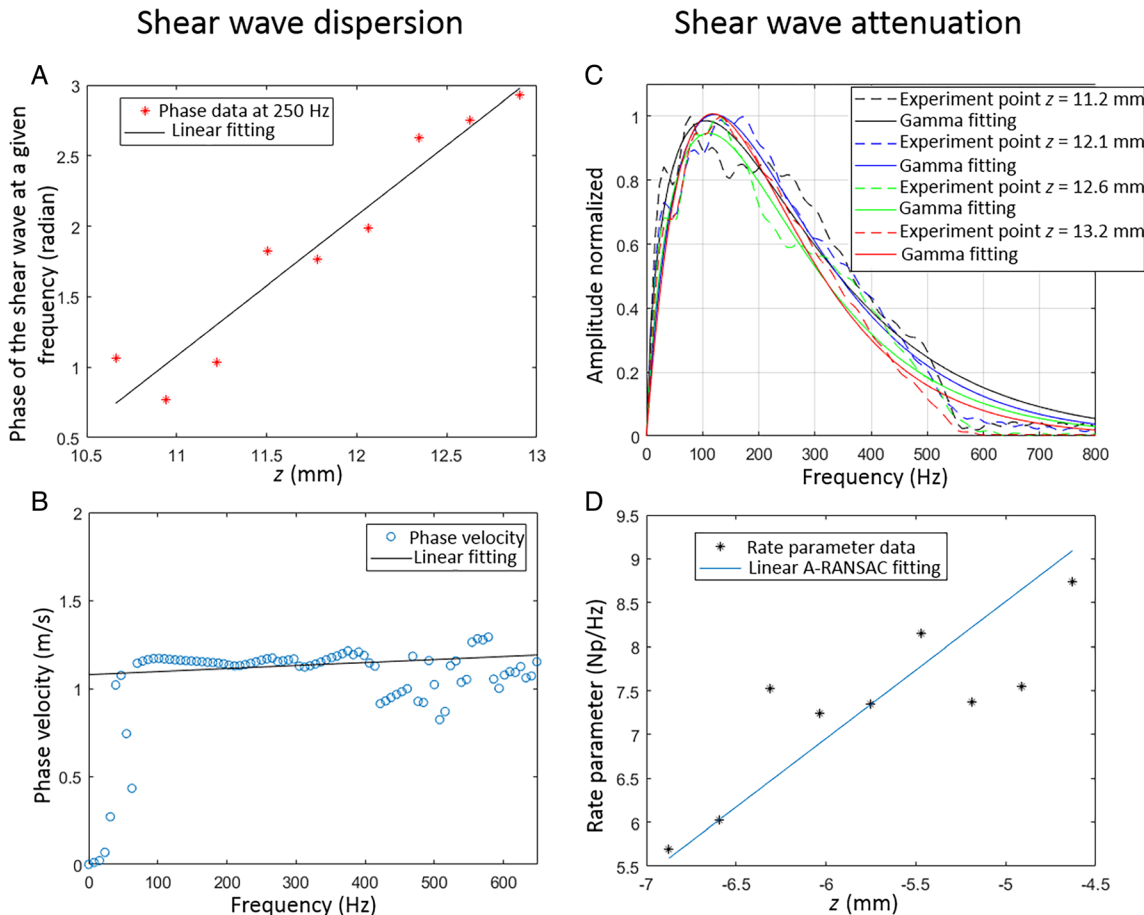


multiple peaks, as shown in Figure 4. The number of peaks depends on resonance properties¹⁴ and they were calculated for each pixel of the selected ROI. To investigate this phenomenon further, the frequency of the main resonant peak (f_1), its width at half maximum (w_1), and, if multiple peaks appeared, the average distance (d) between their frequency pairs was computed for ROI #1. Moreover, to better understand the impact of material properties on f_1 , w_1 , and d , these parameters were plotted for different gel inclusion diameters or as a function of the Young modulus of the blood clot inclusion. Coefficients of variation of each of these three parameters over the ROI were also computed.

Statistics

For gel phantoms, analyses of variance (ANOVA) with multiple pairwise comparisons (Tukey tests) were used to compare the number of peaks, and values of f_1 , w_1 , and d between different inclusion diameters. ANOVA tests were also used to compare the effect of changing the ROI size and position (ie, ROI #1, #2, and #3) on R^2 of the gamma fitting, SW dispersion, and SW attenuation computations. For phantoms with blood clot inclusions, linear mixed effect models (LMM) were considered to evaluate the relation between dependent variables f_1 , w_1 , and d , and the inclusion independent variable Young modulus. To account for repeated data acquisitions

Figure 3. Visual examples of the computation of the shear wave dispersion and shear wave attenuation. The phase velocity at a given frequency is computed by fitting the phase of the shear wave velocity over displacement (panel A). The shear wave dispersion is computed by fitting the phase velocity over frequencies (panel B). In panel C, amplitude spectra are plotted at different space points and fitted by gamma distributions. In panel D, the shear wave attenuation is computed as the slope (using the A-RANSAC linear fitting method) of the rate parameter of all gamma fittings over distances. The data used for this plot correspond to the blood clot inclusion of porcine #19.



over the 110-minute time period, a random intercept was included in the LMM for each pig blood sample. ANOVAs with pairwise comparisons were also used to compare elasticity (Young modulus), SW dispersion and SW attenuation values at 30 different time points. The Kolmogorov–Smirnov test was performed before ANOVA to confirm that data were normally distributed.

Results

Gel Phantom Inclusions

The number of spectral peaks is reported inside the three ROIs for different inclusion diameters in Figure 5, A–D. The two-way ANOVA revealed a statistically significant effect ($P < .001$) of the inclusion diameter and selected ROIs on the number of peaks. Detailed results on those numbers can be found in Figure 5E with significant pairwise differences provided on the graph. For ROI #1, the number of peaks was statistically different between all diameters (the homogeneous phantom can be considered as an infinite diameter inclusion, $P < .001$). The number of peaks between the 6-mm inclusion and all other configurations showed significant differences for ROI #2 ($P < .001$) and ROI #3 ($P < .001$). For all ROIs, the number of peaks was higher when the inclusion

diameter was smaller. For all inclusions (6, 12, and 18 mm), the number of peaks for ROI #1 was higher than for ROI #2 and #3 ($P < .001$), whereas no differences were observed between ROI #2 and #3. Notice the absence of resonance (ie, a single spectral peak) for the homogeneous phantom.

Figure 6A summarizes the effect of the inclusion diameter on f_1 , w_1 , and d . Because those parameters are related to the amplitude spectrum and resonance phenomena, the ROI #1 was selected for those results to maximize the number of resonant peaks. One-way ANOVA tests showed statistically significant differences of dependent variables f_1 , w_1 , and d for the different inclusion diameters ($P < .001$). Multiple pairwise comparisons showed significant increases in f_1 between 6, 12, and 18 mm diameters versus no inclusions ($P < .001$). For w_1 , all comparisons showed significant differences ($P < .001$). The same observation was made for d ($P < .01$). Coefficients of variation (CV, standard deviation divided by the mean) of each parameter are displayed in Figure 6B. For the three parameters, the CV decreased as the diameter increased (the homogeneous phantom can be considered as an infinite diameter), except for d for the diameter of 18 mm.

The median and percentiles of the coefficient of determination R^2 related to the precision of the gamma fitting used for SW attenuation computation were calculated for the 3 ROIs of the homogeneous

Figure 4. Example of displacement amplitude spectra. **A**, A single peak amplitude spectrum with a least squared fitting (in red) used in the revisited frequency shift method. **B**, The same fitting method as in A was applied to a multiple peaks amplitude spectrum. Parameter w_1 corresponds to the width of the first peak f_1 . Parameters d_1 , d_2 and d_3 are distances between frequency peaks in the case of resonances.

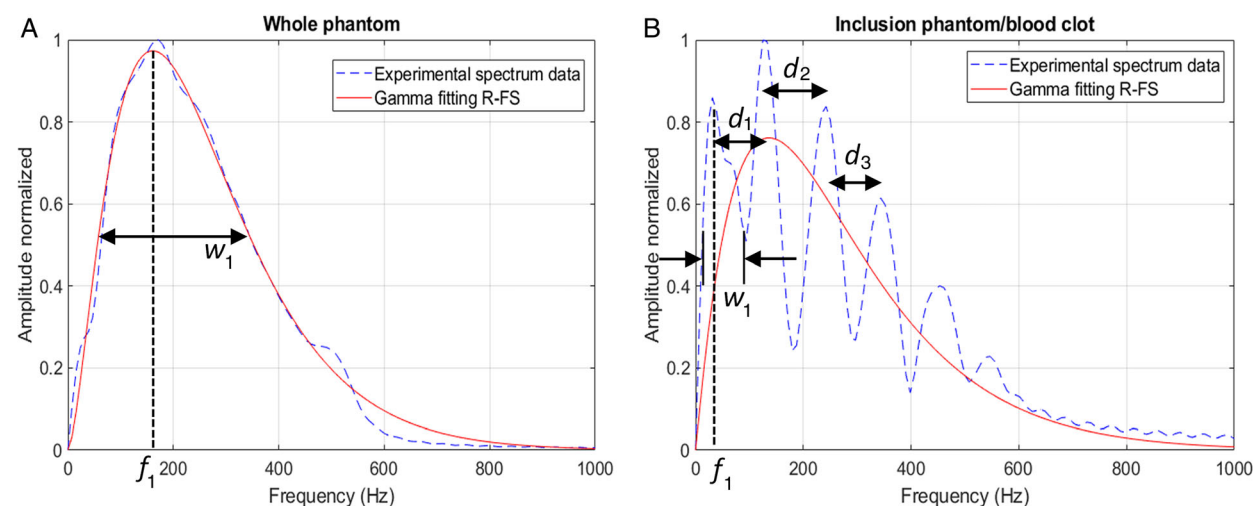
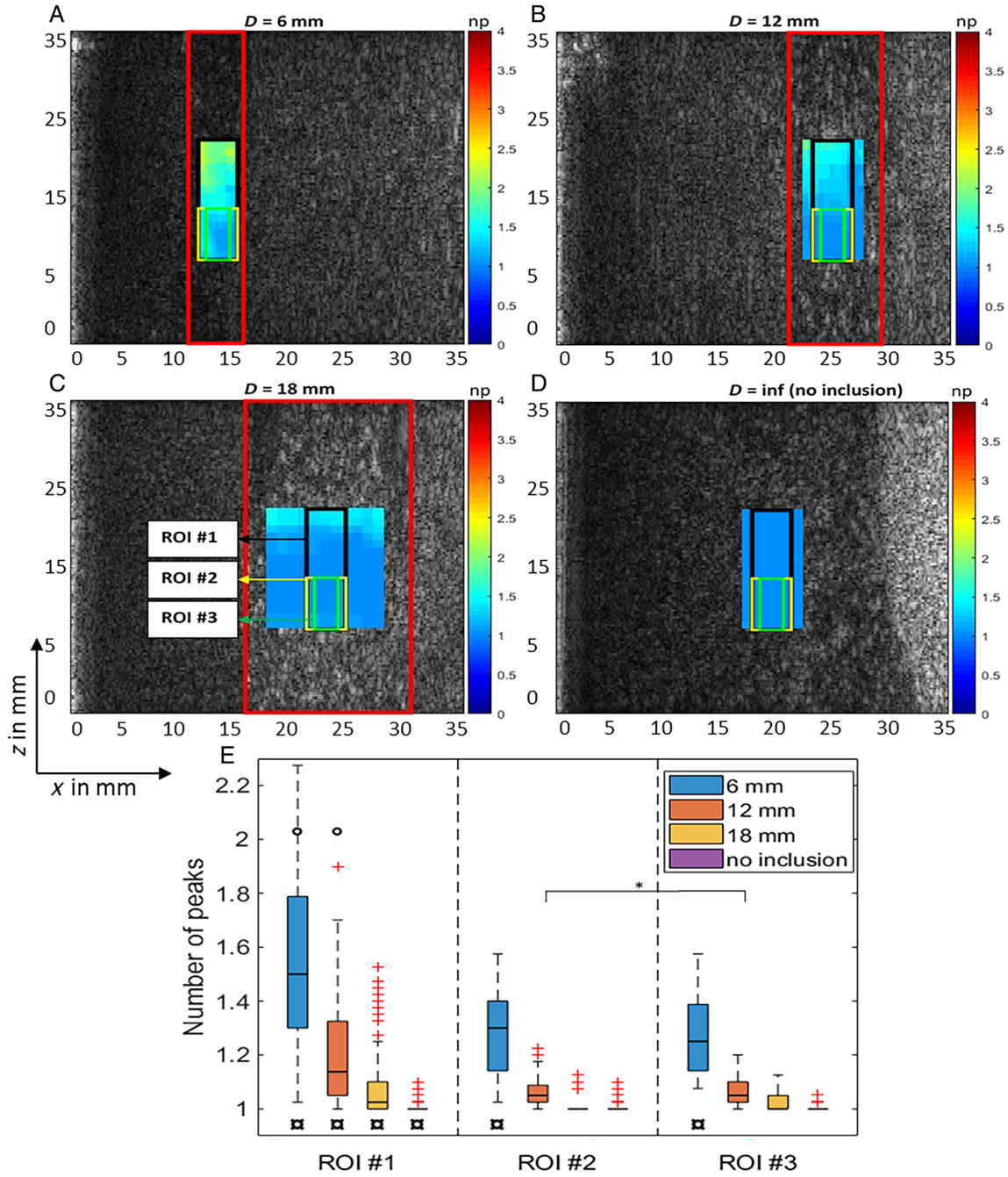


Figure 5. A–D. The number of peaks (np) in amplitude spectra of inclusions with different diameters. The three ROIs are represented, black for ROI #1, yellow for ROI #2, and green for ROI #3. Red rectangles represent the size and position of the inclusion. **E.** The number of peaks over ROIs with different diameters. Symbol α indicates that the box presents significant differences (at $P < .001$) with all other color boxes of the same ROI. Symbol \circ indicates that the box presents significant differences (at $P < .001$) with all other ROI boxes of the same diameter (same color). Symbol * indicates significant differences at $P \leq .05$.



phantom, and the 12-mm gel inclusion phantom (Figure 7). A R^2 close to 1 means that the fitting is good. This coefficient was significantly higher for the homogeneous phantom ($P < .001$), which had no multiple resonant peaks, than for the inclusion phantom (all ROIs combined). In the case of the gel inclusion, ROIs #2 and #3 had better fitting accuracy than ROI #1 ($P < .001$).

The elasticity of the homogeneous soft gel phantom and that of the inclusion were 2.24 ± 0.02 kPa and 1.96 ± 0.02 kPa, respectively; both gels were made with the same recipe. The elasticity of the surrounding phantom (with soft inclusions) was 9.49 ± 0.37 kPa. The SW dispersion and SW attenuation were calculated inside the homogeneous gel phantom and inside the gel inclusion of 12 mm for the three ROIs (boxplots are given in Figure 8). Dispersions (Figure 8A) were lower for the homogeneous phantom ($P < .001$), and between ROI #2 and ROI #1 and #3 for the inclusion ($P < .005$). SW attenuation (Figure 8B) was lower for the homogeneous phantom ($P < .001$), and between ROI #1 and ROI #2 and #3 for the inclusion ($P < .001$).

Blood Clot Inclusions

Clot properties were assessed for 110 minutes with measurements done every 4 minutes. Parameters in Figure 9 were averaged on a total of 20 blood clots

(one per pig). The mean Young modulus increased over time (Figure 9A, $P < .001$). The frequency and width of the first spectral peak (f_1 and w_1) and the mean distance between resonant peaks (d) were averaged over the ROI #1 for each time point to obtain single values reported in Figure 9B–D, respectively. Each color represents a different porcine blood

Figure 7. Coefficients of determination R^2 of the gamma fitting used for shear wave attenuation computation. On each box, the central mark indicates the median, and the bottom and top edges of the box indicate the 25th and 75th percentiles, respectively. Outliers are represented with the “+” red marker. Boxes of R^2 are plotted for the different ROIs in the case of the homogeneous phantom (purple), and for the 12-mm gel inclusion phantom (orange). The symbol * represents $P < .001$.

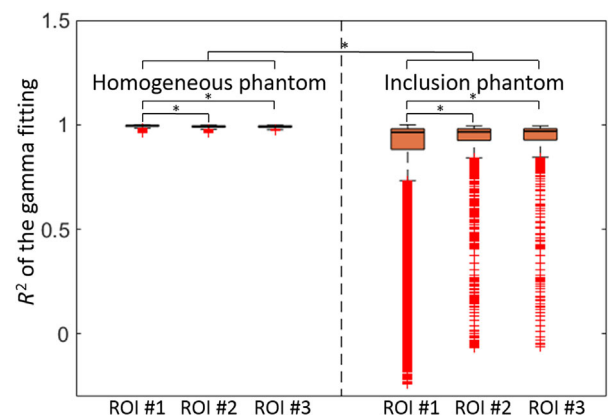
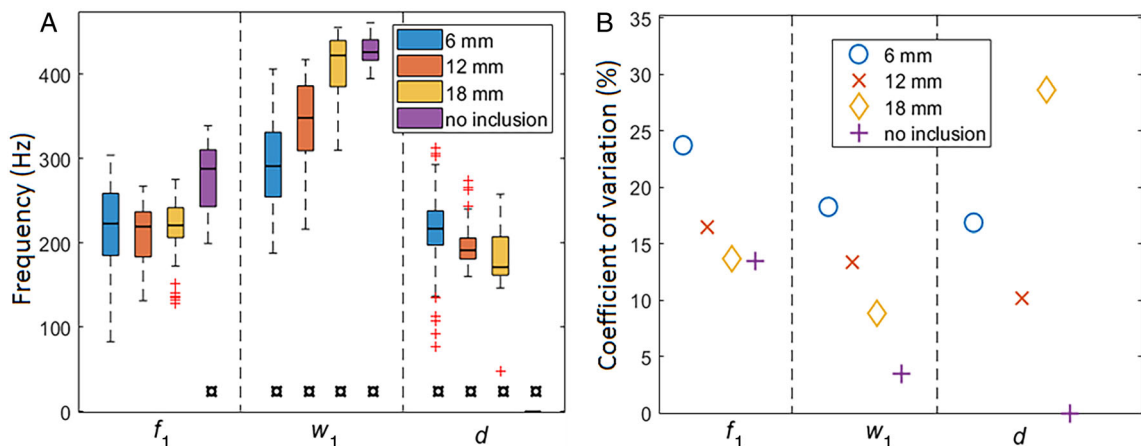


Figure 6. A. The effect of the inclusion diameter on f_1 (the position of the first peak of the amplitude spectrum, left), w_1 (the width at half maximum of the first frequency peak, center), and d (the mean distance between peaks, right). Symbol α means that the box presents significant differences (at $P \leq .01$) with all other color boxes for the same parameter. **B.** Coefficients of variation for f_1 (left), w_1 (center), and d (right), corresponding to data shown in A.



sample. Statistically significant increases ($P < .001$) of f_1 , w_1 , and d as a function of the blood clot Young modulus were observed. Goodness-of-fit parameters R^2 of linear models were 0.77, 0.60, and 0.48 for f_1 , w_1 , and d , respectively.

The SW dispersion and SW attenuation were computed within the ROI #3 to minimize the impact of resonant peaks. The dispersion decreased over time ($P < .001$), as displayed in Figure 10A. Pairwise comparisons revealed higher dispersions between 0 to 4 minutes compared with values after 24 minutes. The dispersion at 8 minutes was also significantly higher than values from 32 to 54 minutes, and 68 to 100 minutes. The SW attenuation is shown in Figure 10B. The SW attenuation decreased over time ($P < .001$). Multiple pairwise comparisons showed higher values at 0, 4, 8, and 12 minutes compared with all other measurements after 30 minutes. The mean and standard deviation of R^2 related to the precision of the gamma fitting were 0.95 ± 0.06 in the case of blood clots over ROI #3.

Discussion

This work aimed to study geometrical and biomechanical effects of confined cylindrical inclusions on

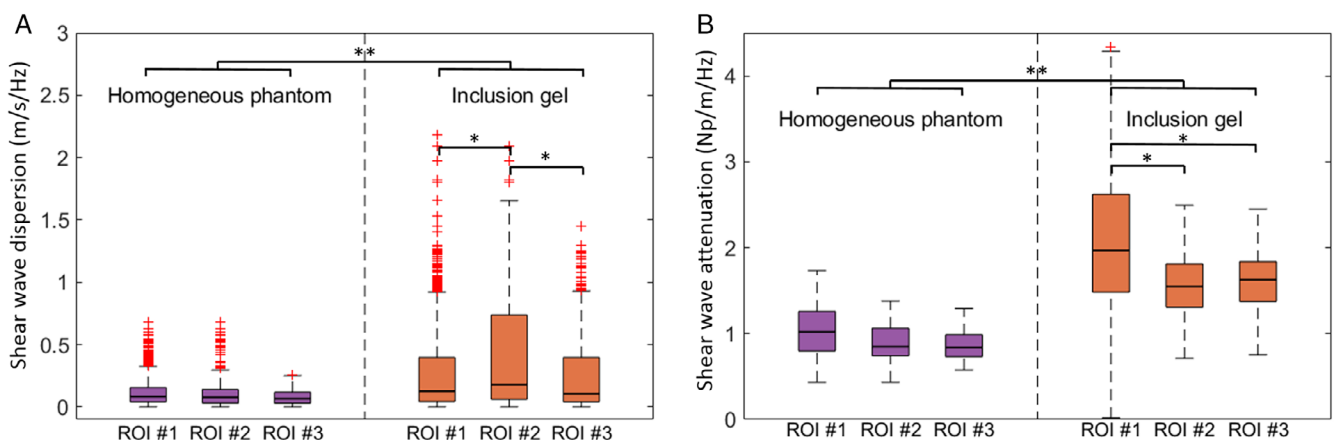
SW properties. Blood clot mimicking gel and coagulating blood inclusions were assessed in vitro.

Gel Phantom Experiments

The number of SW spectral peaks was studied for gel inclusions of different diameters, ROI size, and positions. One hypothesis was that the presence of multiple peaks is related to mechanical resonances of soft inclusions,¹⁴ and that the resonance is caused by the propagation and interaction of SWs with the inclusion boundary and surrounding tissue. During data analysis, we also observed that in a central region of the inclusion and close to acoustic radiation pushes, resonances did not have time to occur. According to Figure 5E, a smaller inclusion diameter resulted in a higher number of peaks in amplitude spectra. The three ROIs were selected to observe spatial differences and regions where resonances were most important. The significant decrease in the number of peaks between ROI #1 and ROIs #2 and #3 supports the fact that resonances were less present near acoustic pushes.

Hadj Henni et al⁶⁰ showed amplitude spectra with multiple peaks corresponding to natural resonant frequencies of a sphere subjected to torsional waves. They excited the material with an external vibrator at the first resonant frequency, assuming that this frequency would maximize the magnitude of

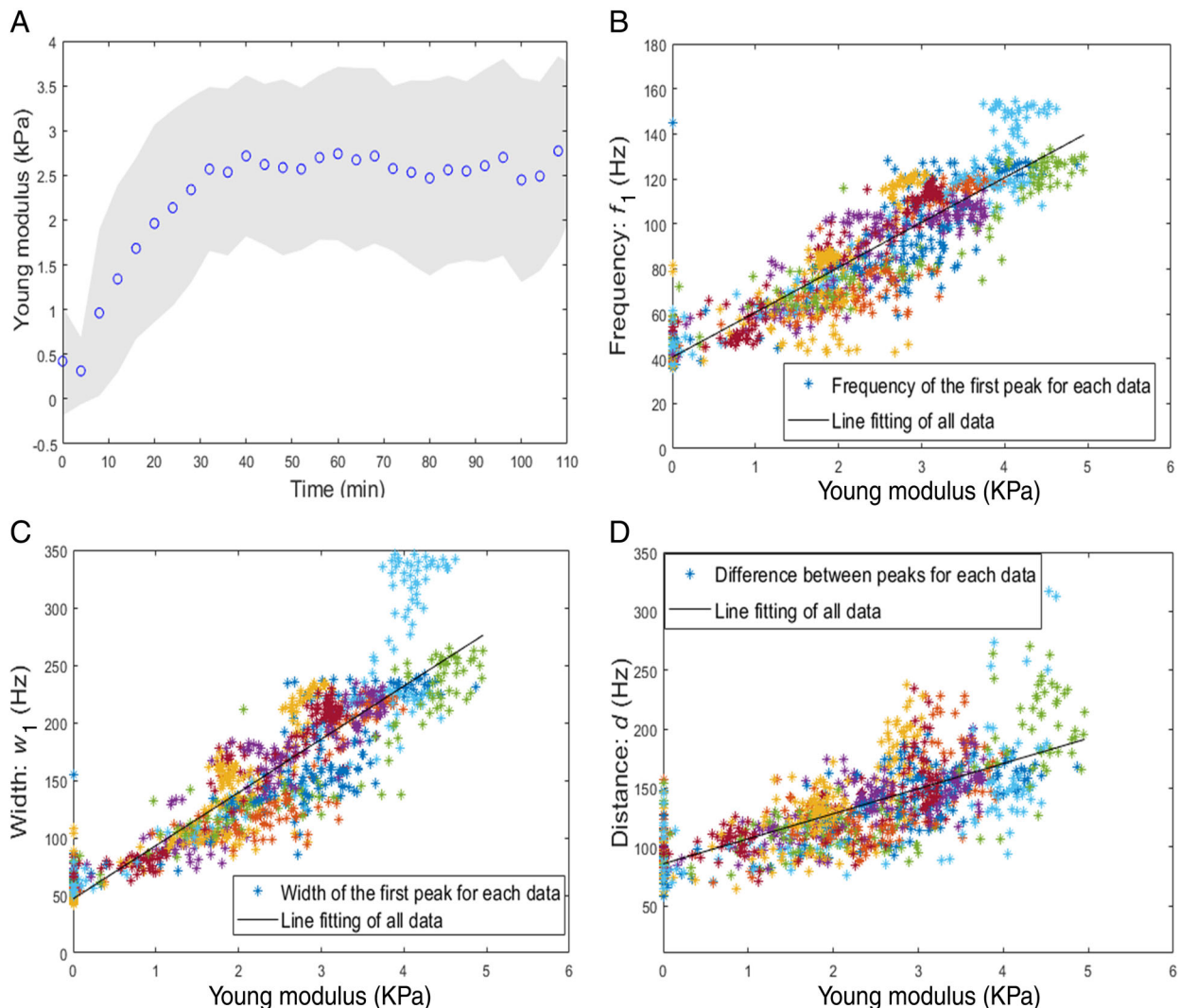
Figure 8. A, Shear wave dispersion and **B**, shear wave attenuation comparison between no inclusion (homogeneous phantom) and the gel inclusion for the 3 ROIs. Significant differences between the homogeneous phantom and the phantom inclusion were found ($P < .001$, as highlighted by the symbol **). Significant differences between ROIs were found in the inclusion gel ($P < .005$), as highlighted by the symbol *. On each box, the central mark indicates the median, and the bottom and top edges of the box indicate the 25th and 75th percentiles, respectively. Outliers are represented with the “+” red marker.



displacements. In our case, selecting a given frequency was not possible because SWs were induced by ultrasound pushes resulting in wideband signals (see Figure 4). One intuitive hypothesis could be that f_1 , w_1 , and d would increase with the inclusion diameter since fewer peaks would appear in a given frequency range. However, this hypothesis seems to go against results simulated by Bhatt et al.¹⁶ They found that the frequency and half-width of the first resonant

peak decreased as the diameter increased from 6 to 16 mm. The decreases were not linear and close to a plateau at 16-mm diameter for both parameters. They also linked parameters f_1 and $w_{1/2}$ (half-width of the spectral peak) to the elasticity and viscosity of inclusions using simulations, and observed a better correlation between f_1 and the elasticity and between $w_{1/2}$ and the viscosity.¹⁶ In their case, the inclusion was imaged longitudinally, and acoustic pulses were

Figure 9. A, Blue dots represent means and the gray area standard deviations over 20 blood clots showing a significant increase over time ($P < .001$). B–D, Colors correspond to different porcine samples. Amplitude spectrum parameters f_1 (the position of the first peak of the amplitude spectrum), w_1 (the width at half maximum of the first peak), and d (the mean distance between peaks) for 20 blood clots in vitro. Significant increases were found for the 3 spectral parameters ($P < .001$). R^2 was calculated as an assessment of the goodness-of-fit ($R^2 = .77$ for f_1 , 0.60 for w_1 , and 0.48 for d).



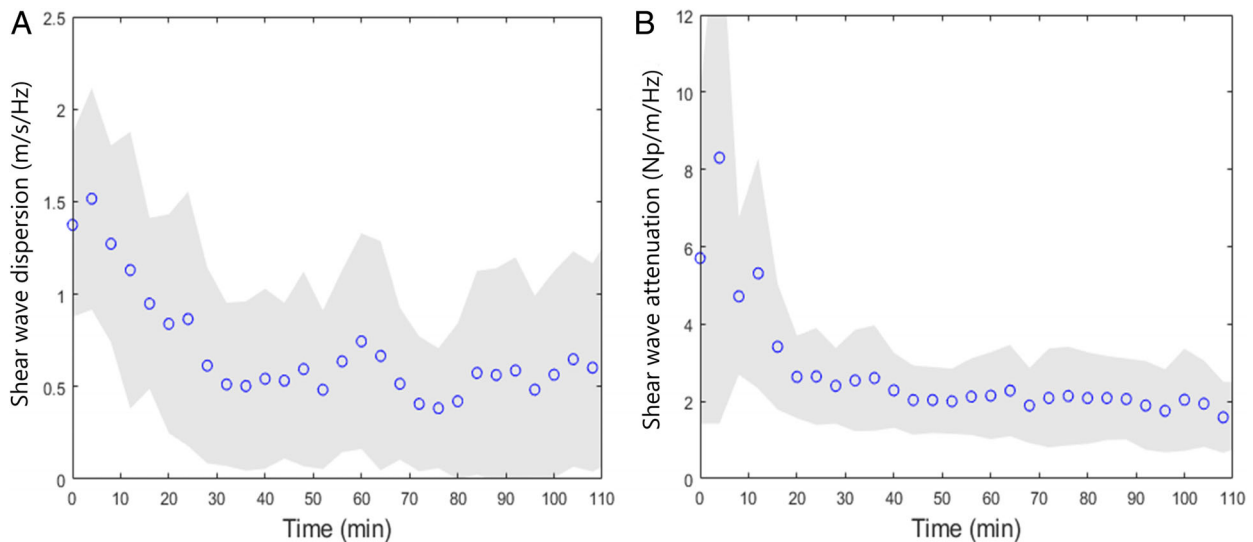
performed outside the inclusion. Multiple peaks were not found in their study, so their simulations do not take into account observations in Figure 4. In our study, no significant difference was found between the different inclusion diameters for f_1 ; however, f_1 was significantly larger for the gel phantom without any inclusion ($P < .001$) than other phantoms with inclusions. This result may be explained by the variability of datasets, which was more important for the smaller inclusion diameter. Significant increases were found for w_1 between all configurations. Decreases of d were also reported between configurations; the presence of more peaks in the same frequency range reduced the distance between them. Coefficients of variation were also reported and decreased as the diameter of the inclusion was increased for all spectral parameters (except d at the diameter of 18 mm). The high CV for d for the inclusion diameter of 18 mm could be explained in part by the lower multiple peak number in the ROI. The CV analyses could emphasize the difficulty of computing particle displacement velocity spectrum-related parameters (f_1 , w_1 , d , and SW attenuation) when reducing the diameter of a soft inclusion.

Soft homogeneous phantom gels and gel inclusions were prepared following the same recipe. However, gelation was different; the gel phantom was

poured into an 800 mL square container and then placed in a refrigerator to solidify. On the other hand, the gel inclusion was poured in a hole into a cold stiffer surrounding gel and placed in the refrigerator. Small volume-dependent gelation time changes may have caused different elastic properties of phantoms.

Figure 7 that showed the coefficient of determination R^2 confirmed the selection of ROI #3 to minimize the impact of resonant spectral peaks on SW attenuation computation (R^2 was significantly higher for ROI #3 than for ROI #1). The SW dispersion and SW attenuation of the homogeneous phantom showed no significant difference for the 3 ROIs. However, they were significantly higher in the inclusion phantom than in the homogeneous phantom. These higher values for the 3 ROIs may also be due to volume-dependent gelation times affecting viscosity. The calculation of the dispersion is based on the assessment of the SW speed with frequency, so the resonance phenomenon (and therefore the selection of ROIs) had less impact. The calculation of the SW attenuation appeared more accurate (smaller standard deviations) in ROIs #2 and #3 of the inclusion phantom, likely because fewer resonant spectral peaks were present in those ROIs. SW attenuation of the same order of magnitude were reported on homogeneous phantoms made with gelatin (5%), xanthan gum

Figure 10. **A**, Shear wave dispersion over time (all data pooled). **B**, Shear wave attenuation over time (all data pooled). Blue circles represent mean values and gray areas standard deviations over 20 blood clots. Significant global effects (decrease) were found for both parameters ($P < .001$) using ANOVA tests.



(0.1–0.5%), and sigmacell (1.5%).³³ Notice on Figure 8 the higher standard deviations for the SW dispersion than for the SW attenuation in the inclusion gel for ROIs #2 and #3, suggesting a higher precision of this latter viscosity-related measurement.

Blood Clot Experiments

The mechanisms that occur during the 2 hours of coagulation reflect the behavior of an acute thrombus composed of red blood cells, platelets, and fibrin strands.⁶¹ An in vivo thrombus becomes chronic after several days/weeks and is characterized by the presence of collagen, a higher Young modulus, and greater resistance to treatment than an acute thrombus.⁶² Acute thrombi are known to be more likely to embolize and create complications.^{63,64} The type and duration of treatment therefore depend on its age, and one of the aims of this study was to characterize the clot age with new parameters such as the SW dispersion and SW attenuation.

The hematocrit was set to 40% to mimic the red blood cell concentration of healthy individuals. Lowering the hematocrit has a known impact on the blood clot Young modulus^{52,53}; therefore, its effect on resonance parameters might deserve to be studied in the future. The diameter of the blood clot inclusion was set to 12 mm, which is larger than venous clots in lower limbs but similar to those in the common iliac and inferior vena cava.⁶⁵ As displayed in Figure 5, the selection of smaller blood clots to better mimic lower limb conditions would have emphasized resonant spectral peaks. As noticed, SW attenuation computed over the ROI #3 provided a mean R^2 value of 0.95 close to the R^2 computed for the 12-mm gel inclusion within ROI #3 (Figure 7), which confirms the robustness of the results.

Previous studies have also shown stiffening of blood clots over time.^{9,12,16,45,46,66–68} This increase is a characteristic of clot aging. However, under clinical conditions, patients, once diagnosed, are treated with anticoagulants, and no time-varying trend in Young modulus has been observed.⁵⁰ The variability, characterized by the standard deviations, reflects the difference in coagulation between pigs. Parameters that may have played a role in this variability include the sex of the pigs, which was not specified, and the time between blood sampling and the start of the experiments, which could vary from a few minutes to 1 hour.

The increase of f_1 , w_1 , and d with Young modulus shows that these resonance parameters are dependent on clot properties. The geometry in our study described a longitudinal view with SWs propagating along the clot. In Bhatt et al¹⁶ study, the imaging of the clot was done with a transverse view; nevertheless, parameters f_1 and $w_{1/2}$ showed similar behaviors in their simulations as in our in vitro results (ie, an increase with rigidity). These findings link resonance parameters to the elastic property of the medium, suggesting that high Young modulus materials propagate SWs at higher frequencies and with a larger bandwidth than a medium with a lower Young modulus. If we consider peaks following the first one as resonant harmonics, an increase in d is a consequence of an increase in f_1 . In Bhatt et al,¹⁶ they did not report multiple peaks, it may be due to the transverse view used in their study. Notice in panels B to D of Figure 9 the significant variability in Young moduli close to 0 kPa. Panel A in the same figure shows very low Young moduli at the start of the experiments ($t = 0$ and 4 minutes). The still-liquid blood was poured into the phantom at $t = 0$ and SWs did not propagate (or propagated very little), increasing the noise in the associated amplitude spectra.

This study also reported the SW dispersion and SW attenuation of blood clots. The blood, via the coagulation cascade, goes from a liquid state to a gel state in a few minutes. The clot structure becomes denser over time,^{69–71} especially with the fibrin strand mesh compressing red blood cells and platelets. Plasma is also extracted from the clot.^{70,72,73} We expected that these phenomena would decrease the dispersion and the attenuation of SWs over time because a more compact and dense clot may tend to be less viscous than a still semi-liquid clot. The decrease in the SW dispersion and SW attenuation of clots during the first 20 minutes reflects this clotting process. ROI #3 was chosen to calculate viscosity-related parameters (SW dispersion and SW attenuation) to reduce resonances seen in Figures 4 and 5. Because clots are biological viscoelastic tissues, it was expected that there would be SW dispersion^{74,75} during clotting (ie, an increase of the phase velocity over frequency, as observed in Figure 10A). Dispersion values are similar in magnitude to results reported by Huang et al⁵² (0.5–1.5 m/s/kHz for us compared with ≈ 0.9 m/s/kHz for them, as estimated from their

Figure 7). Clinical ultrasound scanners can now calculate SW dispersion. We evaluated from Figure 10 the average of the coefficients of variation for the SW dispersion (0.80 ± 0.20) and SW attenuation (0.52 ± 0.11). Because of the lower variability of SW attenuation, it could substitute or improve SW dispersion for tissue characterization.

This study focused on the characterization of cylindrical blood clots in vitro. However, the shape of blood clots in vivo is not necessarily cylindrical, but takes the shape of the vein (or artery) in which they form. Moreover, the total occlusion of a vein (or artery) is not systematic⁷⁶ and partially occluding clots with different geometries may exist. The resonance of SWs observed in our study may likely occur in vivo. An in-depth study of the effect of different clot shapes on resonance phenomena would be necessary for future works, both in vitro and in vivo.

Since the Young modulus was calculated using the group velocity, and resonance phenomena are observed in amplitude spectra, we assumed that resonances did not affect the Young modulus computation. However, other methods for calculating the Young modulus could have been considered (guided waves,⁷⁷ phase velocity,⁵⁹ reverberant shear waves³⁴), and an assessment of the potential impact of spectral resonances would need to be conducted.

Limitations

The pig selection and rearing conditions, feeding, sex, and time between blood collection and experiments could not be controlled as they were part of a protocol external to this study. A more precise control of these conditions and the use of coagulation tests as a priori information could have reduced the impact of these confounders and variations between individuals for measured parameters.

The clot geometry was chosen to be cylindrical for practical reasons related to the experimental condition (easy shape to model, practical to extract the clot from the phantom inclusion), and because this shape approximates in vivo conditions. However, before using the SW dispersion or SW attenuation in vivo, additional studies would deserve to be conducted. Since Bhatt et al¹⁶ did not report multiple resonant peaks in the transverse view, adding this image orientation for SW attenuation computation could be of interest. It may also emphasize the anisotropic behavior of blood clots.

In our experimental design, the Young modulus of the inclusion was lower than that of the surrounding medium. This condition corresponds to acute thrombi, and consequently differences in Young modulus between the blood clot inclusion and the surrounding medium may no longer be the same in the case of chronic blood clots with expected higher Young moduli. This difference may also be emphasized under in vivo conditions. Moreover, the surrounding medium (here a phantom) was homogeneous and way larger than the endothelial wall. Flow phantoms with a mimicking vessel wall and a heterogeneous layered structure with different Young moduli would better reflect in vivo conditions (ie, endothelial wall, collagen and elastin, muscles, and surrounding tissues).

Conclusion

Characterizing clots by their age through ultrasound measurements might help to differentiate between acute and chronic thrombi, and impact their clinical management. In this study, the Young modulus, SW dispersion, and SW attenuation were reported for phantoms embedding clotting blood. The cylindrical shape of blood clots favored the appearance of resonances, characterized by multiple peaks on amplitude spectra. With good ROI selection, the impact of resonances could be diminished. In addition, SW dispersion and SW attenuation varied over time, demonstrating their ability to characterize the evolution of blood clots.

Data Availability Statement

The data that support the findings of this study are available from the corresponding author upon reasonable request.

References

1. Onur MR, Poyraz AK, Ucak EE, et al. Semiquantitative strain elastography of liver masses. *J Ultrasound Med* 2012; 31:1061–1067.
2. Ophir J, Cespedes I, Ponnekanti H, Yazdi Y, Li X. Elastography: a quantitative method for imaging the elasticity of biological tissues. *Ultrasound Imaging* 1991; 13:111–134.

3. Varghese T. Quasi-static ultrasound elastography. *Ultrasound Clin* 2009; 4:323–338.
4. Grajo JR, Barr RG. Strain elastography for prediction of breast cancer tumor grades. *J Ultrasound Med* 2014; 33:129–134.
5. Carlsen JF, Ewertsen C, Lönn L, Nielsen MB. Strain elastography ultrasound: an overview with emphasis on breast cancer diagnosis. *Diagnostics* 2013; 3:117–125.
6. Gennisson JL, Defieux T, Fink M, Tanter M. Ultrasound elastography: principles and techniques. *Diagn Interv Imaging* 2013; 94:487–495.
7. Sigrist RMS, Liao J, El Kaffas A, Chammas MC, Willmann JK. Ultrasound elastography: review of techniques and clinical applications. *Theranostics* 2017; 7:1303–1329.
8. Ozturk A, Grajo JR, Dhyani M, Anthony BW, Samir AE. Principles of ultrasound elastography. *Abdom Radiol* 2018; 43:773–785.
9. Mfoumou E, Tripette J, Blostein M, Cloutier G. Time-dependent hardening of blood clots quantitatively measured in vivo with shear-wave ultrasound imaging in a rabbit model of venous thrombosis. *Thromb Res* 2014; 133:265–271.
10. Evans A, Whelehan P, Thomson K, et al. Quantitative shear wave ultrasound elastography: initial experience in solid breast masses. *Breast Cancer Res* 2010; 12:1–11.
11. Durmaz F, Gultekin MA. Efficacy of shear wave elastography in the differentiation of acute and subacute deep venous thrombosis. *Ultrasound Q* 2021; 37:168–172.
12. Zemzemi C, Phillips M, Vela DC, et al. Effect of thrombin and incubation time on porcine whole blood clot elasticity and rt-PA susceptibility. *Ultrasound Med Biol* 2022; 48:1567–1578.
13. Zaleska-Dorobisz U, Kaczorowski K, Pawlusi A, Puchalska A, Inglot M. Ultrasound elastography – review of techniques and its clinical applications. *Adv Clin Exp Med* 2014; 23:645–655.
14. Hadj Henni A, Schmitt C, Cloutier G. Shear wave induced resonance elastography of soft heterogeneous media. *J Biomech* 2010; 43:1488–1493.
15. Schmitt C, Montagnon E, Henni AH, Qi S, Cloutier G. Shear wave induced resonance elastography of venous thrombi: a proof-of-concept. *IEEE Trans Med Imaging* 2013; 32:565–577.
16. Bhatt M, Montagnon E, Destrempes F, et al. Acoustic radiation force induced resonance elastography of coagulating blood: theoretical viscoelasticity modeling and ex vivo experimentation. *Phys Med Biol* 2018; 63:065018.
17. Laurent S, Cockcroft J, van Bortel L, et al. Expert consensus document on arterial stiffness: methodological issues and clinical applications. *Eur Heart J* 2006; 27:2588–2605.
18. Schmitt C, Soulez G, Maurice RL, Giroux MF, Cloutier G. Noninvasive vascular elastography: toward a complementary characterization tool of atherosclerosis in carotid arteries. *Ultrasound Med Biol* 2007; 33:1841–1858.
19. Cloutier G, Cardinal MHR, Ju Y, et al. Carotid plaque vulnerability assessment using ultrasound elastography and echogenicity analysis. *Am J Roentgenol* 2018; 211:847–855.
20. Marais L, Pernot M, Khettab H, et al. Arterial stiffness assessment by shear wave elastography and ultrafast pulse wave imaging: comparison with reference techniques in normotensives and hypertensives. *Ultrasound Med Biol* 2019; 45:758–772.
21. Roy-Cardinal MH, Destrempes F, Soulez G, Cloutier G. Assessment of carotid artery plaque components with machine learning classification using homodyned-K parametric maps and elastograms. *IEEE Trans Ultrason Ferroelectr Freq Control* 2019; 66:493–504.
22. Sandrin L, Fourquet B, Hasquenoph JM, et al. Transient elastography: a new noninvasive method for assessment of hepatic fibrosis. *Ultrasound Med Biol* 2003; 29:1705–1713.
23. De Ledinghen V, Vergnion J. Transient elastography (FibroScan). *Gastroenterol Clin Biol* 2008; 32:58–67.
24. Bercoff J, Tanter M, Fink M. Supersonic shear imaging: a new technique for soft tissue elasticity mapping. *IEEE Trans Ultrason Ferroelectr Freq Control* 2004; 51:396–409.
25. Gennisson JL, Defieux T, Macé E, et al. Viscoelastic and anisotropic mechanical properties of in vivo muscle tissue assessed by supersonic shear imaging. *Ultrasound Med Biol* 2010; 36:789–801.
26. Eby SF, Song P, Chen S, et al. Validation of shear wave elastography in skeletal muscle. *J Biomech* 2013; 46:2381–2387.
27. Nightingale K, Soo MS, Nightingale R, Trahey G. Acoustic radiation force impulse imaging: in vivo demonstration of clinical feasibility. *Ultrasound Med Biol* 2002; 28:227–235.
28. Bruno C, Minniti S, Bucci A, Pozzi MR. ARFI: from basic principles to clinical applications in diffuse chronic disease—a review. *Insights Imaging* 2016; 7:735–746.
29. Li GY, Cao Y. Mechanics of ultrasound elastography. *Proc R Soc A Math Phys Eng Sci* 2017; 473:20160841.
30. Defieux T, Gennisson JL, Bercoff J, Tanter M. On the effects of reflected waves in transient shear wave elastography. *IEEE Trans Ultrason Ferroelectr Freq Control* 2011; 58:2032–2035.
31. Lipman SL, Rouze NC, Palmeri ML, Nightingale KR. Evaluating the improvement in shear wave speed image quality using multi-dimensional directional filters in the presence of reflection artifacts. *IEEE Trans Ultrason Ferroelectr Freq Control* 2016; 63:1049–1063.
32. Lipman SL, Rouze NC, Palmeri ML, Nightingale KR. Impact of acoustic radiation force excitation geometry on shear wave dispersion and attenuation estimates. *Ultrasound Med Biol* 2018; 44:897–908.
33. Yazdani L, Bhatt M, Rafati I, Tang A, Cloutier G. The revisited frequency-shift method for shear wave attenuation computation and imaging. *IEEE Trans Ultrason Ferroelectr Freq Control* 2022; 69:2061–2074.

34. Parker KJ, Ormachea J, Zvietcovich F, Castaneda B. Reverberant shear wave fields and estimation of tissue properties. *Phys Med Biol* 2017; 62:1046–1061.
35. Nenadic IZ, Qiang B, Urban MW, et al. Attenuation measuring ultrasound shearwave elastography and in vivo application in post-transplant liver patients. *Phys Med Biol* 2017; 62:484–500.
36. Kijanka P, Urban MW. Two-point frequency shift method for shear wave attenuation measurement. *IEEE Trans Ultrason Ferroelectr Freq Control* 2019; 67:483–496.
37. Nightingale K, McAleavey S, Trahey G. Shear-wave generation using acoustic radiation force: in vivo and ex vivo results. *Ultrasound Med Biol* 2003; 29:1715–1723.
38. Chen S, Fatemi M, Greenleaf JF. Quantifying elasticity and viscosity from measurement of shear wave speed dispersion. *J Acoust Soc Am* 2004; 115:2781–2785.
39. Bernard S, Kazemirad S, Cloutier G. A frequency-shift method to measure shear-wave attenuation in soft tissues. *IEEE Trans Ultrason Ferroelectr Freq Control* 2017; 64:514–524.
40. Barry CT, Mills B, Hah Z, et al. Shear wave dispersion measures liver steatosis. *Ultrasound Med Biol* 2012; 38:175–182.
41. Parker KJ, Partin A, Rubens DJ. What do we know about shear wave dispersion in normal and steatotic livers? *Ultrasound Med Biol* 2015; 41:1481–1487.
42. Zhang X, Zheng R, Jin J, et al. US shear-wave elastography dispersion for characterization of chronic liver disease. *Radiology* 2022; 305:597–605.
43. Cetinic I, de Lange C, Simr Y, et al. Ultrasound shear wave elastography, shear wave dispersion and attenuation imaging of pediatric liver disease with histological correlation. *Children* 2022; 9:692.
44. Brum J, Bernal M, Gennisson JL, Tanter M. In vivo evaluation of the elastic anisotropy of the human Achilles tendon using shear wave dispersion analysis. *Phys Med Biol* 2014; 59:505–523.
45. Schmitt C, Hadj Henni A, Cloutier G. Characterization of blood clot viscoelasticity by dynamic ultrasound elastography and modeling of the rheological behavior. *J Biomech* 2011; 44:622–629.
46. Gennisson JL, Lerouge S, Cloutier G. Assessment by transient elastography of the viscoelastic properties of blood during clotting. *Ultrasound Med Biol* 2006; 32:1529–1537.
47. Santini P, Esposto G, Ainora ME, et al. Ultrasound elastography to assess age of deep vein thrombosis : a systematic review. *Diagn Interv Imaging* 2023; 13:2075.
48. Mumoli N, Mastroiaco D, Giorgi-Pierfranceschi M, et al. Ultrasound elastography is useful to distinguish acute and chronic deep vein thrombosis. *J Thromb Haemost* 2018; 16:2482–2491.
49. Mercado-Shekar KP, Kleven RT, Aponte Rivera H, et al. Effect of clot stiffness on recombinant tissue plasminogen activator lytic susceptibility in vitro. *Ultrasound Med Biol* 2018; 44:2710–2727.
50. Bosio G, Zenati N, Destrepes F, et al. Shear wave elastography and quantitative ultrasound as biomarkers to characterize deep vein thrombosis in vivo. *J Ultrasound Med* 2022; 41:1807–1816.
51. Hendley SA, Dimov A, Bhargava A, et al. Assessment of histological characteristics, imaging markers, and rt-PA susceptibility of ex vivo venous thrombi. *Sci Rep* 2021; 11:22805.
52. Huang CC, Chen PY, Shih CC. Estimating the viscoelastic modulus of a thrombus using an ultrasonic shear-wave approach. *Med Phys* 2013; 40:042901.
53. Liu HC, Abbasi M, Ding YH, et al. Characterizing blood clots using acoustic radiation force optical coherence elastography and ultrasound shear wave elastography. *Phys Med Biol* 2021; 66:035013.
54. Li N, Tous C, Dimov IP, et al. Quantification and 3D localization of magnetically navigated superparamagnetic particles using MRI in phantom and swine chemoembolization models. *IEEE Trans Biomed Eng* 2022; 69:2616–2627.
55. Tozaki M, Saito M, Joo C, et al. Ultrasonographic tissue quantification of the breast using acoustic radiation force impulse technology: phantom study and clinical application. *Jpn J Radiol* 2011; 29:598–603.
56. Ouared A, Montagnon E, Kazemirad S, et al. Frequency adaptation for enhanced radiation force amplitude in dynamic elastography. *IEEE Trans Ultrason Ferroelectr Freq Control* 2015; 62:1453–1466.
57. Garcia D, Le Tarnec L, Muth S, et al. Stolt's f-k migration for plane wave ultrasound imaging. *IEEE Trans Ultrason Ferroelectr Freq Control* 2013; 60:1853–1867.
58. Loupas T, Powers JT, Gill RW. An axial velocity estimator for ultrasound blood flow imaging, based on a full evaluation of the doppler equation by means of a two-dimensional autocorrelation approach. *IEEE Trans Ultrason Ferroelectr Freq Control* 1995; 42:672–688.
59. Deffieux T, Montaldo G, Tanter M, Fink M. Shear wave spectroscopy for in vivo quantification of human soft tissues visco-elasticity. *IEEE Trans Med Imaging* 2009; 28:313–322.
60. Hadj Henni A, Schmitt C, Trop I, Cloutier G. Shear wave induced resonance elastography of spherical masses with polarized torsional waves. *Appl Phys Lett* 2012; 100:1–6.
61. Aslan A, Barutca H, Ayaz E, et al. Is real-time elastography helpful to differentiate acute from subacute deep venous thrombosis? A preliminary study. *J Clin Ultrasound* 2018; 46:116–121.
62. Stanford SN, Sabra A, D'Silva L, et al. The changes in clot microstructure in patients with ischaemic stroke and the effects of therapeutic intervention: a prospective observational study. *BMC Neurol* 2015; 15:1–8.
63. Xie H, Kim K, Aglyamov SR, et al. Staging deep venous thrombosis using ultrasound elasticity imaging: animal model. *Ultrasound Med Biol* 2004; 30:1385–1396.
64. Czaplicki C, Albadawi H, Partovi S, et al. Can thrombus age guide thrombolytic therapy? *Cardiovasc Diagn Ther* 2017; 7:S186–S196.
65. Bosson JL, Riachi M, Pichot O, Michoud E. Diameters of acute proximal and distal deep venous thrombosis of the lower limbs: proposed reference values of ultrasonography. *Int Angiol* 1998; 17:260–267.

66. Bernal M, Gennisson JL, Flaud P, Tanter M. Shear wave elastography quantification of blood elasticity during clotting. *Ultrasound Med Biol* 2012; 38:2218–2228.
67. Bernal M, Gennisson JL, Flaud P, Tanter M. Correlation between classical rheometry and supersonic shear wave imaging in blood clots. *Ultrasound Med Biol* 2013; 39:2123–2136.
68. Rayes A, Zhang J, Lu G, et al. Estimating thrombus elasticity by shear wave elastography to evaluate ultrasound thrombolysis for thrombus with different stiffness. *IEEE Trans Biomed Eng* 2023; 70:135–143.
69. Huang CC, Wang SH, Tsui PH. Detection of blood coagulation and clot formation using quantitative ultrasonic parameters. *Ultrasound Med Biol* 2005; 31:1567–1573.
70. Tutwiler V, Litvinov RI, Lozhkin AP, et al. Kinetics and mechanics of clot contraction are governed by the molecular and cellular composition of the blood. *Blood* 2016; 127:149–159.
71. Risman RA, Abdelhamid A, Weisel JW, Bannish BE, Tutwiler V. Effects of clot contraction on clot degradation: a mathematical and experimental approach. *Biophys J* 2022; 121:3271–3285.
72. Carr ME. Development of platelet contractile force as a research and clinical measure of platelet function. *Cell Biochem Biophys* 2003; 38:55–78.
73. Cines DB, Lebedeva T, Nagaswami C, et al. Clot contraction: compression of erythrocytes into tightly packed polyhedra and redistribution of platelets and fibrin. *Blood* 2014; 123:1596–1603.
74. Sugimoto K, Fuminori M, Hisashi O, et al. Clinical utilization of shear wave dispersion imaging in diffuse liver disease. *Ultrasonography* 2019; 39:3–10.
75. Blackstock DT, Atchley AA. Fundamentals of physical acoustics. *J Acoust Soc Am* 2001; 109:1274–1276.
76. Pan FS, Tian WS, Luo J, et al. Added value of two-dimensional shear wave elastography to ultrasonography for staging common femoral vein thrombi. *Med Ultrason* 2017; 19:51–58.
77. Lee WN, Chang EJJ, Guo Y, Wang Y. Experimental investigation of guided wave imaging in thin soft media under various coupling conditions. *Ultrasound Med Biol* 2018; 44:2821–2837.